

1 **WIND-RETRIEVAL FROM MULTI-ANGLE**
2 **BACKSCATTER LIDAR PROFILES THROUGH**
3 **ANISOTROPIC AEROSOL STRUCTURES**

4
5
6
7
8
9
10
11
12
13
14
15
16
17

Sergio Tomás¹ and Francesc Rocadenbosch^{2,3}

Institut de Ciències de l’Espai (ICE-CSIC/IEEC), Campus UAB, E-08193

Barcelona, Spain.

²Dept. of Signal Theory and Communications, Remote Sensing Lab.

(RSLAB), Universitat Politècnica de Catalunya (UPC), E-08034 Barcelona,

Spain.

³Institut d’Estudis Espacials de Catalunya (IEEC-CRAE), E-08034 Barcelona,

Spain.

¹ *Corresponding author:* Sergio Tomás, Institut de Ciències de l’Espai (ICE-CSIC/IEEC), Campus UAB, E-08193 Barcelona, Spain. E-mail: tomas@ice.cat

Abstract

18
19

20 A wind-retrieval correlation method for backscatter-lidar scanning schemes consisting of a
21 few profiling sounding lines of sight (LOS) is mathematically formulated in matrix-solution
22 form under general anisotropic atmospheric conditions and convective boundary layer
23 scenarios. The method assumes the frozen atmosphere model and works with temporal cross-
24 correlations functions that do not need to be maximized. The method also applies to the well-
25 known case of slant scans based on the multiple-angle azimuth technique (horizontal wind
26 retrievals). A first application of the method to a 1064-nm wavelength case example is
27 presented for a 40-deg elevation, two-angle azimuth scan where horizontal wind speed and
28 wind direction are retrieved.

29

30 1. Introduction

31 Wind lidar (light detection and ranging) remote sensing has key applications in fields such as
32 meteorology (weather forecasting), environmental science (pollutant trajectories), and
33 aeronautics (wind-shear early-warning systems). Lidars remotely profile the motion of
34 atmospheric scatterers, namely molecules and aerosols, which can be applied to retrieve the
35 mean wind vector. Equipped with a scanning system, lidars can be used to map the horizontal
36 or even the vertical wind components, rather than just yielding the wind-radial projection on
37 the sounding line of sight (LOS) (Rocadenbosch, 2003).

38 Doppler wind lidars use both coherent and direct-detection techniques (edge and fringe
39 techniques; Comerón et al., 2010) to measure the radial velocity of the wind field along the
40 sensor LOS, from the Doppler frequency shift of the return radiation both in ground and
41 space-borne wind-profiling applications. Prominent missions include NASA's LAWS (Lidar
42 Atmospheric Wind Sounder, LAWS, 1987), ESA's ALADIN (Atmospheric Laser Doppler
43 Instrument, ALADIN, 1989), and NOAA's (National Oceanic and Atmospheric
44 Administration) Doppler lidar projects (Hall et al., 1984; Clifford et al., 1994; Huffaker and
45 Hardesty, 1996). Backscatter lidars use pattern correlation analysis of aerosol inhomogeneities
46 (i.e., persistent contrastable patterns having a correlated spatial structure) swept away by the
47 wind to identify pattern similarities at specific time/range lags. In contrast to Doppler wind
48 lidars, backscatter lidars are simple, low-cost, and yield reasonable wind speed accuracies and
49 spatial inversion resolutions inside the atmospheric boundary layer (ABL) (Hooper and
50 Eloranta 1986; Matsui et al. 1990; Piironen and Eloranta, 1995; Buttler et al. 2001). However,

51 two unwanted effects alter this straightforward “correlation” concept: spatial anisotropy of the
52 aerosol pattern and wind turbulence. So far, two primary wind-retrieval methodologies have
53 been developed: point-correlation methods and spatial-correlation methods.

54 ***Point-correlation methods*** antecede lidar invention, and were first applied to the study
55 of ionospheric irregularities in downward propagating radio waves, such as horizontal drifts
56 and time shifts, between fading curves observed from three or more ground-spaced receiving
57 antennas (Briggs et al., 1950; Philips and Spencer, 1955; Briggs, 1968). This family of
58 methods (see Holloway et al., 1997, for a review) requires triangulation of three sounding
59 points on the same horizontal plane, and an analysis of the time series at these correlation
60 points in the form of *auto- and cross-correlations*. Adaptation of these methods to lidar
61 atmospheric sounding involves at least three non-coplanar LOS close to zenith pointing so that
62 three points lie on each horizontal plane along the vertical direction, hence replicating the
63 triangulation philosophy of radio-antenna measurements (Zuev et al., 1977; Clemesha et al.,
64 1981; Kolev et al., 1988; Morley et al., 2010).

65 From this work (known as Full Correlation Analysis, FCA) two simplifying
66 assumptions are applied: (i) the “frozen” pattern assumption (i.e., that the pattern details
67 remain invariant as it moves; Stull (1988)) and (ii) the pattern *isotropy* assumption (i.e., that
68 the range lag between two separate points yielding a given correlation value is independent of
69 the direction chosen). Inclusion of random changes in the pattern and of anisotropic conditions
70 has also been considered (Phillips and Spencer, 1955; Briggs, 1968).

71 ***Spatial-correlation methods*** were developed mainly for atmospheric lidar sounding.
72 Correlation along a lidar LOS at low-elevation angles for retrieving the radial wind

73 component was the first example of spatial correlation analysis (Eloranta et al., 1975). Later
74 on, additional LOS were added to derive the transversal wind component from *cross-*
75 *correlation function estimation* in the time domain (Kunkel et al., 1980). The radial wind
76 component was also estimated in the frequency domain (Sroga et al., 1980), including
77 anisotropy effects for this component only (Hooper and Eloranta, 1986).

78 In these spatial-correlation methods, the lidar is basically configured as a transit-time
79 wind profiler to scan back and forth at two, three, or more LOS. The LOS can be arranged in
80 closely-spaced azimuth angles at a fixed elevation angle, so that the wind vector is
81 decomposed into two orthogonal components: one along the LOS of the lidar (radial direction)
82 and another perpendicular to the LOS, and, therefore, horizontal to the ground. In contrast to
83 FCA, these spatial-correlation methods are used to retrieve the transversal-wind component by
84 means of a correlation-function model based on advection by a random wind field, in a
85 conceptually similar manner to previous works on solar-wind measurements (Little and Ekers,
86 1971). Under simplified conditions (e.g., isotropic and “frozen” atmospheres), a simple
87 algorithm represents the *maximization of the correlation function* (Kunz 1996; Buttler et al.,
88 2001), which permits identifying the time- or range-lag where aerosol pattern similarities
89 occur.

90 *Advanced measurement techniques* since the 1990s have further developed point- and
91 spatial-correlation methods. The *vertical sounding* approach was enhanced with more LOS for
92 refined point-correlation analysis (Matsui et al., 1990; Sugimoto et al., 1998), which gave rise
93 to a complete conical vertical scanning and the so-called kymematical analysis (Schwemmer,
94 1998; Wilkerson et al., 2002). Another technique combines multi-laser sounding with a

95 frequency-domain analysis of the correlation function (Kovalev and Eichinger, 2004). In each
96 of these cases, a vertical profile of the wind is obtained assuming *isotropy* and a *frozen*
97 atmosphere.

98 Multiple-azimuth-LOS *horizontal scanning* was also extended to the so-called “large-
99 area” scanning, where an area-correlation analysis is applied. For example, Sasano et al.
100 (1982), Schols and Eloranta (1992), and Mayor and Eloranta (2001) used a “large-area”
101 pattern matching method (e.g., a lidar sensor scanning a circular sector at a given elevation
102 angle) based on the two-dimensional correlation function of the aerosol pattern measured at
103 two different times. This basically means obtaining a volume image of the horizontal wind
104 field instead of a simple vertical profile (Schols and Eloranta, 1992; Piironen and Eloranta,
105 1995). The main drawback of these “large-area” scanning methods is the reduced scanning
106 time available in practice, which usually is not fast enough to sweep the area twice before the
107 aerosol distribution decorrelates. With a frozen atmosphere, a moving observer with the mean
108 wind would see the aerosol pattern undistorted. As a natural evolution, further work has
109 measured the anisotropic and turbulent properties of eddy structures (Young and Eloranta,
110 1995; Mayor and Eloranta, 2001; Mayor, 2010) to the point of beginning to use optical flow
111 methods instead of correlation to retrieve high-spatial-resolution wind fields (on the order of
112 one vector in a 10x10-m grid every 30 s; Derian et al., 2010; Mayor et al., 2013).

113 Wind-retrieval methods relying on temporal/spatial-lag *maximization* of the aerosol-
114 pattern correlation function are *not suitable* for scan schemes with only a few LOS. A primary
115 reason for this is the limited number of baselines that can be formed in the atmospheric
116 volume of interest for velocity inversion (hereafter the “velocity-inversion volume”), where a

117 baseline is defined as the difference position vector between two measurement points for a
118 common/different LOS. In the case of temporal optimization (time-lag solution maximizing
119 the correlation function), the anisotropy of the medium introduces an *apparent direction* of
120 drift that distorts the inverted wind solution with the anisotropic dominant direction, causing
121 “*false-velocity*” estimates. In the case of spatial optimization, and though this method yields
122 correct wind-velocity estimates under anisotropic conditions, a densely sampled volume is
123 needed to solve for the baseline maximising correlation. Besides, numerical solution of the
124 maximization problem is always cumbersome, for it involves quadratic and cross-product
125 terms of the wind components. Further, estimation of the correlation maximum is not an easy
126 task in scenes with moderate-to-low signal-to-noise ratios (SNR).

127 ***In this paper***, we mathematically formulate a tri-dimensional wind-retrieval temporal
128 correlation method under general anisotropic conditions, which requires at least six
129 independent baselines from three non-coplanar LOS. Departing from this generalized
130 formulation, the method is aimed at lidar systems with scanning capabilities limited to such
131 multiple-azimuth scanning at low-to-mid elevation angles. The method combines both
132 aforementioned philosophies. Thus, *point correlation* is applied to time series obtained from
133 low-elevation, multiple-azimuth scanning measurements (typical of *spatial-correlation*
134 methods). As a result, several advantages arise: First, and foremost, is that both *wind* and
135 *anisotropic* information are retrieved, since spatially anisotropic aerosol structures can readily
136 be detected by means of backscatter lidar (Mayor et al., 2003). In doing so, the only
137 requirement is that the atmosphere is assumed to be piece-wise homogeneous in height. That
138 is, the anisotropic properties remain the same in each vertical “layer” or atmospheric

139 “velocity-inversion volume”. Second is that the retrieval procedure does not rely on
140 maximization of the temporal correlation function (as previously discussed, this may lead to
141 false-velocity estimates under anisotropic conditions) or on “a priori” selection of a baseline
142 aligned with the true wind direction. In contrast, the method relies on densely-sampled
143 measurement points along the LOS of the lidar from which a subset of suitable wind-
144 estimation baselines is selected. And third, a matrix-oriented, linear solution of the problem is
145 presented.

146 The method presented is, in fact, a type of FCA. The method is intended for low
147 turbulence situations where the mean wind velocity is much higher than the velocity standard
148 deviation caused by shifting-wind aerosol concentration fluctuations. In this case, Taylor’s
149 hypothesis (Taylor, 1938; Stull, 1988) holds (i.e., aerosol patterns are advected without any
150 change in their shape as if they were “frozen”). This is a sensible approximation followed in
151 practice even when working with advanced backscatter lidars (Sugimoto et al., 1998; Buttler
152 et al., 2001; Wilkerson et al., 2003; Kovalev and Eichinger, 2004).

153 This paper is organized as follows: in Section 2, an introduction of the coordinate
154 systems inherent to the problem and aerosol-pattern correlation fundamentals is presented.
155 Section 3 (core section) includes the mathematical formulation of the wind and anisotropy-
156 matrix retrieval method, and Section 4 presents a first simplified application case of the
157 method for a two-LOS scanning scheme. Finally, concluding remarks are given in Section 5.
158 Supplementary material (on-line accesible) shows a review of aerosol-pattern correlation
159 models and discusses the limitations of the classic approach based on time/space
160 maximization of the correlation function.

161 2. Fundamentals

162 2.1. Coordinate systems

163 Consider an aerosol pattern, $N_{aer}(\mathbf{X}, t)$ moving with a mean wind velocity, \mathbf{U} , and the
164 coordinate geometry of Fig.1a. The mean-wind vector defines the *wind-relative* coordinate
165 system $(\hat{\mathbf{x}}_1, \hat{\mathbf{x}}_2, \hat{\mathbf{x}}_3)$; namely, the along-wind, cross-wind and vertical coordinate vectors), where
166 the mean wind at a height Z is assumed horizontally invariant and defined as

167
$$\mathbf{U}(Z) = U_1 \hat{\mathbf{x}}_1 + U_3 \hat{\mathbf{x}}_3, \tag{1}$$

168 with $U_3 \ll U_1$.

169 The wind-relative coordinate system is defined so that the cross-wind mean
170 component, U_2 , is identically zero. Formally, the total wind is the superposition of the mean
171 wind component (advective transport) plus the turbulent one, the latter being responsible for
172 eddy diffusion and changes in the aerosol pattern as it moves. Because of the “frozen”
173 atmosphere assumption (Sect. 1), the turbulent component will be neglected in what follows
174 so that the total wind vector is the same as the mean wind vector, \mathbf{U} (\mathbf{U} in the wind-relative
175 coordinate system, or alternatively, \mathbf{V} in the absolute coordinate system; see Fig.1b and Table
176 1).

177 In this work, a minimum of two sensing LOS are assumed for the scanning backscatter
178 lidar. The LOS are arranged around a LOS-symmetry axis (case of multiple LOS) or bisectrix
179 of the angle between the two LOS (case of two LOS), used as a “reference” line for the
180 scanning scheme. Such schemes are typically the two-, three- and five-angle azimuth scan and

181 the four-angle square scan. The absolute coordinate system $(\hat{\mathbf{x}}, \hat{\mathbf{y}}, \hat{\mathbf{z}})$, or *instrument-coordinate*
182 *system* (Fig.1b), is defined relative to the lidar in such a way that $\hat{\mathbf{y}}$ is the horizontal
183 projection of the reference line of the two LOS depicted (positive when $\hat{\mathbf{y}}$ forms an acute
184 angle with the plane containing the two LOS); $\hat{\mathbf{x}}$ is defined orthogonal to $\hat{\mathbf{y}}$ and following a
185 positive trihedral, and $\hat{\mathbf{z}} = \hat{\mathbf{x}}_3$ is the vertical axis. θ and ϕ are, respectively, the azimuth and
186 elevation angles of the two LOS in the absolute coordinate system $(\hat{\mathbf{x}}, \hat{\mathbf{y}}, \hat{\mathbf{z}})$. The origin of both
187 *fixed* coordinate systems coincide ($O(\hat{\mathbf{x}}, \hat{\mathbf{y}}, \hat{\mathbf{z}}) \equiv O'(\hat{\mathbf{x}}_1, \hat{\mathbf{x}}_2, \hat{\mathbf{x}}_3)$) at the intersection point between
188 the horizontal plane at height z and the reference line, so that the wind-relative coordinate
189 system $(\hat{\mathbf{x}}_1, \hat{\mathbf{x}}_2, \hat{\mathbf{x}}_3)$ is the counter clock-wise rotated version of the absolute system $(\hat{\mathbf{x}}, \hat{\mathbf{y}}, \hat{\mathbf{z}})$ by
190 an azimuth angle ϕ_w . In other words, ϕ_w is the wind direction relative to the absolute
191 coordinate system. The rotation transform matrix is given in Table 1. For a three-angle
192 azimuth scan, the pictorial sketch would be similar to that of Fig.1b, with the “reference” line
193 corresponding with the central LOS.

194 2.2. Aerosol pattern correlation

195 2.2.1 SPATIAL CORRELATION FUNCTION

196 The spatial correlation function is a unit-normalised statistical measurement of similarity
197 between two functions at different spatial lags. The spatial correlation function of a static
198 aerosol concentration field, $N_{aer}(\mathbf{X})$ ($\mathbf{U} = \mathbf{0}$), at two separated positions \mathbf{X}_0 and $\mathbf{X}_1 = \mathbf{X}_0 + \boldsymbol{\rho}$
199 in the wind-relative coordinate system $(\hat{\mathbf{x}}_1, \hat{\mathbf{x}}_2, \hat{\mathbf{x}}_3)$ is defined as

$$B(\boldsymbol{\rho}) = \frac{E\left[\left\{N_{aer}(\mathbf{X}_0) - E[N_{aer}(\mathbf{X}_0)]\right\}\left\{N_{aer}(\mathbf{X}_0 + \boldsymbol{\rho}) - E[N_{aer}(\mathbf{X}_0 + \boldsymbol{\rho})]\right\}\right]}{E\left[\left\{N_{aer}(\mathbf{X}_0) - E[N_{aer}(\mathbf{X}_0)]\right\}^2\right]}, \quad (2)$$

201 where E is the expectancy operator representing the statistical average. The terms bracketed
 202 $\{N_{aer}(\mathbf{X}_i) - E[N_{aer}(\mathbf{X}_i)]\}$ $i = 0,1$ stand for the aerosol concentration fluctuations around the
 203 average concentration at position \mathbf{X}_i , and the denominator is a normalization factor.

204 In practice, the aerosol concentration, N_{aer} , is replaced by the range-corrected
 205 backscatter lidar return power $S(R_i) = R_i^2 P(R_i)$, $i = 1..N$ (N is the number of samples along
 206 the LOS). For the single-scattering elastic lidar equation (Measures, 1992), the range-
 207 corrected power is proportional to the product of the atmospheric total-backscatter coefficient
 208 (aerosol plus molecules, $\beta = \beta_{aer} + \beta_{mol}$) and the two-way path atmospheric transmission.
 209 Since 1) in aerosol-dominant regions such as the ABL and, particularly, towards the near
 210 infrared, $\beta \approx \beta_{aer}$, and 2) for a well-mixed atmosphere, transmission is approximately
 211 constant in the correlation volume, the aerosol-concentration approximation above holds
 212 (Collis and Russell, 1976).

213 *2.2.1.1 Formulation of the spatial correlation function in terms of functional models and the* 214 *anisotropy matrix*

215 $B(\boldsymbol{\rho})$ in Eq.(2) attains a maximum value of unity at zero range lag, $\boldsymbol{\rho} = \mathbf{0}$. In standard
 216 correlation analysis, it is assumed that the correlation function follows a monotonically
 217 decreasing behaviour, usually modelled by a Gaussian or exponential model (Ishimaru, 1978).

218 Therefore, contours of the three-dimensional spatial correlation function, $B(\boldsymbol{\rho})$, take the form
 219 of concentric ellipsoidal surfaces. Concentric ellipsoids, rather than spheres, are a
 220 consequence of pattern *anisotropy*, which causes stretching of the contours in one direction.
 221 This direction corresponds with the major axis of the correlation ellipsoid and does not
 222 necessarily coincide with the mean-wind direction (Fig 2). Initial large-scale concentration
 223 gradients and a spatially-variant wind field are responsible for the anisotropy of the aerosol
 224 distributions in the inertial-convective range (Elperin et al., 1996). Thus, wind shear distorts
 225 the aerosol structures directionally as well as enhancing isotropic turbulent diffusion (Stull,
 226 1988). Atmospheric vertical stratification also gives rise to different levels of vertical
 227 correlation along the extent of the ABL, thus showing aspect ratios between the horizontal and
 228 vertical correlation lengths (Doviak et al., 1996).

229 From this basis, it is convenient to express the spatial correlation as

$$230 \quad B(\boldsymbol{\rho}) = f[q(\boldsymbol{\rho})] = (f \circ q)(\boldsymbol{\rho}), \quad (3)$$

231 where f is a monotonically decreasing function model (in this work we have used a simple
 232 exponential decay, see Supplementary Material) and $q(\boldsymbol{\rho})$ is a real positive quadratic form
 233 representing tri-dimensional ellipsoids centered at the origin $O'(\hat{\mathbf{x}}_1, \hat{\mathbf{x}}_2, \hat{\mathbf{x}}_3)$ of the form

$$234 \quad q(\boldsymbol{\rho}) = a\rho_1^2 + b\rho_2^2 + c\rho_3^2 + d\rho_1\rho_2 + e\rho_1\rho_3 + f\rho_2\rho_3. \quad (4)$$

235 It can be shown that the d , e and f terms describe ellipsoid rotation with respect to the
 236 coordinate axes $(\hat{\mathbf{x}}_1, \hat{\mathbf{x}}_2, \hat{\mathbf{x}}_3)$, arising when describing the correlation ellipsoids in a fixed-
 237 observation system. The locus for which the correlation function is equal to one half
 238 ($B(\boldsymbol{\rho}) = 1/2$) is called the ‘‘characteristic ellipsoid’’ (Briggs, 1968).

239 A more convenient form to express the effects of the anisotropy on the correlation
 240 pattern contours is found by rewriting the quadratic form q in terms of the anisotropy matrix,
 241 \mathbf{M} , or

$$242 \quad q(\boldsymbol{\rho}) = \boldsymbol{\rho}^T \mathbf{M} \boldsymbol{\rho} = (\rho_1 \quad \rho_2 \quad \rho_3) \begin{pmatrix} m_1 & m_{12} & m_{13} \\ m_{12} & m_2 & m_{23} \\ m_{13} & m_{23} & m_3 \end{pmatrix} \begin{pmatrix} \rho_1 \\ \rho_2 \\ \rho_3 \end{pmatrix}, \quad (5)$$

243 where superscript "T" means "transposed." In Eq.(5), the main diagonal elements of the
 244 anisotropy matrix, $m_i = \frac{1}{2\rho_{c,i}}$, $i=1,\dots,3$, are one half of the inverse of the characteristic
 245 correlation length associated to the $\hat{\mathbf{x}}_i$ axis, $\rho_{c,i}$. Here, $\rho_{c,i}$ is the length of the semi-principal
 246 axes of the correlation ellipsoid in the wind-relative coordinate system, $(\hat{\mathbf{x}}_1, \hat{\mathbf{x}}_2, \hat{\mathbf{x}}_3)$. The non-
 247 diagonal elements, m_{ij} , stand for the rotations of the principal axis of the correlation ellipsoid
 248 with respect to the wind-relative coordinate system.

249 Scanning area measurements have shown that correlation contours are well-
 250 represented by ellipsoids whose alignment with respect to the wind may be tilted and vary in
 251 height (Mayor et al., 2003). The latter implies that the atmosphere can be modeled by
 252 horizontal layers of a given vertical extent in which the wind field is *approximately* invariant
 253 in both speed and direction. This is the "piece-wise" vertical homogeneous approximation of
 254 the atmosphere outlined in Sect. 1. In each of these layers, both the wind field and the aerosol
 255 concentration field are considered time-stationary and statistically-homogeneous in space
 256 (Ferdinandov and Mitsev, 1982). Therefore, each layer, or "velocity-inversion volume", is
 257 characterised by a unique anisotropy matrix, \mathbf{M} . It is assumed that atmospheric spatial

258 variability does not significantly change the anisotropy matrix during the measurement time,
 259 which is consistent with the frozen-atmosphere hypothesis.

260 For the isotropic case, all three correlation lengths are equal, $\rho_{c,i} = \rho_c$, $i = 1..3$, and
 261 $m_{ij} = 0$. Therefore, \mathbf{M} is proportional to the identity matrix, and Eq.(4) above reduces to a
 262 sphere, $q(\boldsymbol{\rho}) = (\rho_1^2 + \rho_2^2 + \rho_3^2) / 2\rho_c^2$. The isotropic approximation has been used in practice
 263 (Kunkel et al., 1980; Sroga et al., 1980; Matsui et al., 1990) under the assumption that the
 264 average of the remotely-sensed inhomogeneities is isotropically correlated. However, this
 265 approximation cannot be taken for granted because it depends on the measuring scale and,
 266 hence, on the possibility of detecting aerosol concentration gradients.

267 2.2.2 SPACE-TIME CORRELATION FUNCTION MODEL

268 *Generalized model.*- An observer in the wind-relative coordinate system $(\hat{\mathbf{x}}_1, \hat{\mathbf{x}}_2, \hat{\mathbf{x}}_3)$ can make
 269 observations at spaced points and times to compute the space-time correlation function of the
 270 aerosol concentration field. The *generalized model* for the spatio-temporal correlation function
 271 of an atmospheric layer centered at a height, Z , and time delay, τ , between these time
 272 observations is defined by Little and Ekers (1971) as

$$273 \quad R_z(\boldsymbol{\rho}, \tau) = \iiint B[\boldsymbol{\rho} - \mathbf{u}(Z)\tau] p[\mathbf{u}(Z)] du_1 du_2 du_3. \quad (6)$$

274 Here, $\mathbf{u}(Z) = \mathbf{U}(Z) + \mathbf{u}_t(Z)$ is the random wind field, with $\mathbf{U}(Z)$ the mean wind and $\mathbf{u}_t(Z)$
 275 the turbulent random component. $p[\mathbf{u}(Z)]$ is the probability density function (p.d.f.) of the
 276 random wind field (usually Gaussian isotropic), u_1, u_2, u_3 are the wind-speed components, and
 277 subindex Z is a reminder that Eq.(6) is computed over an atmospheric layer centered at height

278 Z and extending from a generic height Z_a to Z_b (“piece-wise” vertical homogeneous
 279 approximation).

280 *Frozen-atmosphere model.*- The practical simplification of Eq.(6) is the frozen-atmosphere
 281 assumption (Stull, 1988). This is to say that the *diffusive* (i.e., turbulent) wind component is
 282 much smaller than the *advective* (mean wind) one (i.e., $\sigma_i^2 \ll U^2$), with σ_i^2 representing the
 283 variance of the turbulent wind, or, formally, that the wind p.d.f. tends to a Dirac’s delta
 284 distribution,

$$285 \quad p(\mathbf{u}) = \delta(u_1 - U_1, u_2 - U_2, u_3 - U_3). \quad (7)$$

286 Substitution of Eq.(7) into Eq.(6) yields the physically obvious result that if the aerosol pattern
 287 is “frozen” the space-time correlation function $R_Z(\boldsymbol{\rho}, \tau)$ (referring to the coordinate system
 288 $(\hat{\mathbf{x}}_1, \hat{\mathbf{x}}_2, \hat{\mathbf{x}}_3)$) is just a translation of the “static” spatial correlation function of the aerosol
 289 pattern, $B(\boldsymbol{\rho})$, by an amount, $\boldsymbol{\rho}_0(Z) = \mathbf{U}(Z)\tau$. That is,

$$290 \quad R_Z(\boldsymbol{\rho}, \tau) = B[\boldsymbol{\rho} - \mathbf{U}(Z)\tau] = f\{q[\boldsymbol{\rho} - \mathbf{U}(Z)\tau]\}, \quad (8)$$

291 where we have used the corresponding form of Eq.(3).

292 Taylor’s hypothesis adds a valuable simplification in the atmospheric description of
 293 aerosol transport, since it relates time and spatial statistics through velocity scaling. The
 294 assumption of the frozen atmosphere (Eq.(8)) is thus required for what follows.

295 2.2.3 SPACE-TIME CORRELATION FUNCTION IN ABSOLUTE COORDINATES

296 From Sect. 2.1 and Table 1, the coordinate transform rotation matrix, $\boldsymbol{\Psi}$, enables us to relate
 297 absolute (lidar)- and relative (wind)-coordinate baseline vectors as

298
$$\mathbf{r} = \Psi(\mathbf{V})\boldsymbol{\rho}. \quad (9)$$

299 In Eq.(9), it is important to note that because the coordinate system $(\hat{\mathbf{x}}_1, \hat{\mathbf{x}}_2, \hat{\mathbf{x}}_3)$ is wind
 300 relative (i.e., defined by the wind angle ϕ_w , see Table 1), determination of Ψ requires
 301 previous retrieval of the wind vector, \mathbf{V} .

302 Re-formulation of the space-time correlation model function of Sect. 2.2.1.1 in
 303 absolute coordinates can simply be done by changing the coordinates of quadratic form, $q(\boldsymbol{\rho})$
 304 (Eq.(3)). Since rotation matrices are symmetric, $q(\boldsymbol{\rho})$ can be expressed in the absolute
 305 coordinate system as

306
$$q(\boldsymbol{\rho}) = \boldsymbol{\rho}^T \mathbf{M} \boldsymbol{\rho} = \mathbf{r}^T \Psi \mathbf{M} \Psi^T \mathbf{r} = \mathbf{r}^T \mathbf{A} \mathbf{r}, \quad (10)$$

307 where

308
$$\mathbf{A} = \Psi \mathbf{M} \Psi^T \quad (11)$$

309 is the anisotropy matrix in absolute coordinates. \mathbf{A} is also positive-defined and symmetric
 310 because Ψ is unitary.

311 By introducing the frozen-atmosphere model of Eq.(8), Eq.(10) takes the form

312
$$q(\boldsymbol{\rho}, \tau) = q(\boldsymbol{\rho} - \mathbf{U}(Z)\tau) = (\mathbf{r}^T - \mathbf{V}^T \tau) \mathbf{A} (\mathbf{r} - \mathbf{V} \tau), \quad (12)$$

313 where $\mathbf{V} = \Psi \mathbf{U}$ is the mean wind vector referenced in the absolute coordinate system.

314 In the wind-retrieval method developed in Sect. 3, the velocity-inversion procedure is
 315 carried out in two steps. First, the anisotropy matrix, \mathbf{A} , is determined and, second, the wind
 316 vector, \mathbf{V} , is determined.

317

318 3. Method

319 3.1. Measured space-time correlation function

320 The space-time cross-correlation (Sect. 2.2.2) from *measured* lidar signals in an atmospheric
 321 aerosol layer (or velocity-inversion volume) centered at a height Z (Fig. 1c) is always
 322 referenced to the “lidar” absolute-coordinate system, and it can be written as

$$323 \quad \Gamma_Z^{pq,ij} = \Gamma_Z(\mathbf{r}_{pq,ij}, \tau) = S_n(\mathbf{R}_{p,i}, t, \theta_p, \phi_p) * S_n(\mathbf{R}_{q,j}, t, \theta_q, \phi_q), \quad (13)$$

324 where $\mathbf{r}_{pq,ij} = \mathbf{R}_{q,j} - \mathbf{R}_{p,i}$. Here, Γ_Z denotes the *measured* correlation function (in contrast to
 325 R_Z , which stands for the *model* correlation function). The pair (θ_k, ϕ_k) , $k = p, q$, stands,
 326 respectively, for the elevation and azimuth angles of the k -th LOS, $\mathbf{R}_{k,i}$, $k = p, q$ is the range
 327 vector to the i -th discrete measurement point on the k -th LOS, and $\mathbf{r}_{pq,ij}$ is the *baseline* or
 328 range-lag vector between the i -th and j -th measurement points, respectively, on the p -th and q -
 329 th LOS (see Fig. 1c). A *baseline* is a vector representing the difference between a pair of
 330 range-bin positions from the available LOS of the lidar instrument in the inversion volume,
 331 which can be seen as a lattice of discrete-point lidar measurements. τ is the time delay and $*$
 332 is the correlation operator.

333 Eq.(13) represents the *temporal correlation associated with the $\mathbf{r}_{pq,ij}$ baseline*, and
 334 $\mathbf{r} = \mathbf{r}_{pq,ij}$ is the absolute coordinate system counterpart of $\boldsymbol{\rho}$ (Eq.(2)) in the “wind” relative-
 335 coordinate system. S_n is the range-corrected lidar return along a given LOS, expressed as a
 336 deviation from its time-average value and normalized by its standard deviation as

337
$$S_n(R_i, t) = \frac{S(R_i, t) - \overline{S(R_i, t)}}{\left\{ \frac{1}{M} \sum_{m=1}^M [S(R_i, t_m) - \overline{S(R_i, t)}]^2 \right\}^{\frac{1}{2}}}, \quad (14)$$

338 where R_i is formally the distance $R_i = |\mathbf{R}_{k,i}|$, m stands for the m -th lidar return, M is number
 339 of lidar records, and the top bar means a time average. Consequently, Γ_z is normalized to
 340 $\Gamma_z(\mathbf{0}, 0) = 1$.

341 For the sake of comparison with Eq.(8), Eq.(13) can be rewritten as

342
$$\Gamma_z(\mathbf{r}, \tau) = S_{n,p}(\mathbf{R}_0, t) * S_{n,q}(\mathbf{R}_0 + \mathbf{r}, t + \tau), \quad (15)$$

343 where we have used $\mathbf{R}_{p,i} = \mathbf{R}_0$ and $\mathbf{R}_{q,j} = \mathbf{R}_{p,i} + \mathbf{r}$ in Eq.(13). The goal of obtaining the
 344 measurement correlation function of Eq.(15), $\Gamma_z(\mathbf{r}, \tau)$, is to *estimate the model correlation*
 345 *function*, $\hat{R}_z(\boldsymbol{\rho}, \tau)$ (Sect. 2.2.2), through

346
$$\Gamma_z(\mathbf{r}, \tau) = \hat{R}_z(\boldsymbol{\rho}, \tau) \Big|_{\boldsymbol{\rho} = \boldsymbol{\Psi}^T \mathbf{r}}, \quad (16)$$

347 from which the wind components and anisotropic parameters can be derived.

348 Eq. (16) warrants some comments. First, a change in coordinates is involved (noted as
 349 $\boldsymbol{\rho} = \boldsymbol{\Psi}^T \mathbf{r}$; Table 1). Because $\Gamma_z(\mathbf{r}, \tau)$ is computed in the lidar-absolute coordinate system,
 350 $(\hat{\mathbf{x}}, \hat{\mathbf{y}}, \hat{\mathbf{z}})$, the first step towards being able to compare both functions is to express the model
 351 correlation function, $R_z(\boldsymbol{\rho}, \tau)$ (Eq. (8)), in the $(\hat{\mathbf{x}}, \hat{\mathbf{y}}, \hat{\mathbf{z}})$ absolute coordinate system, as
 352 described in Sect. 2.2.3. Second, while the model formulation of $R_z(\boldsymbol{\rho}, \tau)$ is 1) continuous in
 353 space, $\boldsymbol{\rho}$, and time, τ , and 2) rooted in the wind-relative coordinate system $(\hat{\mathbf{x}}_1, \hat{\mathbf{x}}_2, \hat{\mathbf{x}}_3)$,

354 $\Gamma_z(\mathbf{r}, \tau)$ is discrete in space, $\mathbf{r}_{pq,ij}$, and time, τ . This is because of the finite number of
 355 baselines in the velocity-inversion volume and inherent time resolution of the lidar sensor.

356 3.2. Retrieval of the anisotropy matrix

357 The space-time correlation evaluated at zero-time delay is the aerosol-pattern spatial
 358 correlation function (Little and Ekers, 1971). From Eq.(8),

$$359 R_z(\boldsymbol{\rho}, 0) = f[q(\boldsymbol{\rho})]. \quad (17)$$

360 In Sect. 3.1, it has been shown that the *measurement* correlation function, $\Gamma_z(\mathbf{r}, \tau)$, and the
 361 *model* correlation function, $R_z(\boldsymbol{\rho}, \tau)$, (the first being an estimate of the second) are analogous
 362 except for a coordinate axis rotation. This rotation relates baseline vector $\boldsymbol{\rho}$ to \mathbf{r} (Table 1),
 363 and causes the quadratic form, q , or “ellipsoid” to take the form (Eq. (10)),

$$364 q(\boldsymbol{\rho}) = \mathbf{r}^T \mathbf{A} \mathbf{r}. \quad (18)$$

365 By substituting Eq. (18) into Eq. (17), Eq. (17) leads to

$$366 R_z(\mathbf{r}, 0) = f(\mathbf{r}^T \mathbf{A} \mathbf{r}). \quad (19)$$

367 To retrieve the anisotropy matrix in Eq. (19), one is interested in the quadratic term,
 368 $\mathbf{r}^T \mathbf{A} \mathbf{r}$, and one uses the fact that model correlation function, $R_z(\mathbf{r}, \tau)$, is estimated from the
 369 measured one, $\Gamma_z(\mathbf{r}, \tau)$. Thus, given the model-correlation decay function, f , from the user’s
 370 side, the anisotropy matrix \mathbf{A} can formally be inverted as

$$371 \mathbf{r}^T \mathbf{A} \mathbf{r} = f^{-1}[\Gamma_z(\mathbf{r}, 0)]. \quad (20)$$

372 In Eq. (20), there are six unknowns inherited from the anisotropy matrix coefficients of
 373 Eq.(5) (recall that \mathbf{A} is the rotated version of \mathbf{M} , Tab. 1) and one single equation. In order to
 374 come up with an over-determined set of equations, we evaluate Eq.(20) above at a set of
 375 $N \geq 6$ baselines, \mathbf{r}_k , $k = 1..N$, from selected pairs of points in the velocity-inversion volume
 376 grid of interest (atmospheric layer at height Z ; see Sect. 4.1 for hints on the selection criteria)
 377 so that

$$378 \quad \mathbf{r}_k^T \mathbf{A} \mathbf{r}_k = f^{-1}[\Gamma_z(\mathbf{r}_k, 0)], \quad k = 1..N. \quad (21)$$

379 $\Gamma_z(\mathbf{r}_k, 0)$ represents the temporal correlation at zero-lag delay for the baselines \mathbf{r}_k , $k = 1..N$.

380 Using that,

$$381 \quad \mathbf{r}^T \mathbf{A} \mathbf{r} = a_{11}x^2 + a_{22}y^2 + a_{33}z^2 + a_{12}xy + a_{13}xz + a_{23}yz \quad (22)$$

382 (counterpart of Eq.(4) in absolute coordinates, see Table 1), and Eq.(21) can be cast into the
 383 $N \times 6$ linear equation system as

$$384 \quad \mathbf{P} \mathbf{a} = \mathbf{b}, \quad (23)$$

385 where

$$386 \quad \mathbf{P} = \begin{bmatrix} x_1^2 & y_1^2 & z_1^2 & 2x_1y_1 & 2x_1z_1 & 2y_1z_1 \\ x_2^2 & y_2^2 & z_2^2 & 2x_2y_2 & 2x_2z_2 & 2y_2z_2 \\ \vdots & \vdots & \vdots & \vdots & \vdots & \vdots \\ x_N^2 & y_N^2 & z_N^2 & 2x_Ny_N & 2x_Nz_N & 2y_Nz_N \end{bmatrix}, \quad \mathbf{a} = \begin{bmatrix} a_{11} \\ a_{22} \\ \vdots \\ a_{23} \end{bmatrix}, \quad \mathbf{b} = \begin{bmatrix} f^{-1}[\Gamma_z(\mathbf{r}_1, 0)] \\ f^{-1}[\Gamma_z(\mathbf{r}_2, 0)] \\ \vdots \\ f^{-1}[\Gamma_z(\mathbf{r}_N, 0)] \end{bmatrix}. \quad (24)$$

387 In Eq.(24), \mathbf{a} is the 6×1 vector reshape of the anisotropy matrix \mathbf{A} (six non-redundant
 388 coefficients inherited from \mathbf{M} , Eq.(5)). For $N \geq 6$, and \mathbf{P} a full-rank matrix, solution of
 389 Eq.(24) is obtained via the pseudo-inverse matrix of \mathbf{P} as $\mathbf{a} = \mathbf{P}^{ps} \mathbf{b} = (\mathbf{P}^T \mathbf{P})^{-1} (\mathbf{P} \mathbf{b})$, which is

390 the solution that minimizes the error norm $\|\mathbf{a} - \mathbf{P}\mathbf{b}\|$ in a mean-squared sense (Barlow, 1999).
391 In order to have a unique solution (\mathbf{P} with rank six), at least six non-parallel baselines are
392 needed, which in turn require at least four non-coplanar points. Once the absolute-coordinate
393 anisotropy matrix, \mathbf{A} , is solved from Eq.(24) above, retrieval of the aerosol anisotropy matrix
394 \mathbf{M} . (Eq.(5)), via Eq.(11) requires the previous retrieval of the wind vector (Sect.3.3). This is
395 because, as outlined in Eq.(9) and Sect.2.1, the coordinate transformation matrix, Ψ , depends
396 on the wind vector ($\Psi = \Psi(\mathbf{V})$, Table 1) via the wind angle, ϕ_w . This procedure must be
397 repeated for each atmospheric layer considered.

398 *3.3. Retrieval of the wind vector*

399 The limitations, and very often unsuitability, of the classic correlation-function maximization
400 method for wind retrievals have been discussed in Sect. 1. A straightforward linear
401 formulation is presented next based on the so-called temporal “correlation intersect method,”
402 which does not require correlation maximization. The proposed method departs from the work
403 of Briggs (1950) on ionospheric returns, and states that the time delay where the *temporal*
404 auto- and cross-correlation functions intersect enables the wind velocity to be inverted
405 independent of turbulence effects (assumption of frozen atmosphere). In a first step, the
406 method is reviewed under the assumption of a one-dimensional ground for illustrative
407 purposes (same as in the reference above). In a second step, we show its extension to the tri-
408 dimensional case.

409 *Correlation analysis without function maximization*

410 In the *one-dimensional case*, $\mathbf{r} = (x, y, z)$ reduces to x and the locus of constant
411 correlation, $R_z(x, \tau) = \text{const.}$, consists of concentric contour ellipses in the (x, τ) domain (see
412 Fig. 3). The space shift or “baseline”, $x = x_{opt}$, maximizing the *spatial* correlation function,
413 given lidar observations separated by a time interval, τ_0 , is also plotted and corresponds with
414 point C ($\left. \frac{dR_z(x, \tau_0)}{dx} \right|_{x=x_{opt}} = 0$). The wind drift velocity is computed as $V = x_{opt}/\tau_0$. In the tri-
415 dimensional case,

$$416 \quad \mathbf{V} = \mathbf{r}_{opt}/\tau_0, \quad (25)$$

417 where \mathbf{r}_{opt} is the baseline maximizing the correlation function (spatial optimization).

418 In Fig. 3, the horizontal line $\tau = \tau_0$ intersects “contour₀” at points A and B , where the
419 correlation function attains the value $R_z(x, \tau) = \text{const}_0$. Contour₀ is such that point A lies on
420 the τ axis and, therefore, point A corresponds with the auto-correlation, $R_z(0, \tau_0)$. Point B
421 corresponds with cross-correlation, $R_z(x, \tau_0)$, with baseline $x = x_0$. Therefore,
422 $R_z(0, \tau_0) = R_z(x, \tau_0) = \text{const}_0$ at time-lag intercept, τ_0 .

423 According to geometrical properties of the rotated contour ellipse, the wind drift
424 velocity is computed as $V = x_0/(2\tau_0)$ (see Sect. 5.iv and Eq. (17) in Briggs, 1950). In other
425 words, given the user baseline, $x = x_0$, maximization of the correlation function is equivalent
426 to finding the time lag, τ_0 , where *temporal* cross-correlation function $R_z(x = x_0, \tau)$ (point B)
427 and *temporal* autocorrelation function, $R_z(0, \tau)$ (point A), intersect. Moreover, because the
428 “correlation intersect method” relies on geometrical properties of the correlation ellipse, it also

429 holds for many other time intersects, including $\tau_{i,1}$ (points A_1, B_1 ; baseline x_1) and $\tau_{i,2}$
 430 (points A_2, B_2 ; baseline x_2). In these cases, the same drift velocity is obtained as

$$431 \quad V = x_0/(2\tau_0) = x_1/(2\tau_{i,1}) = x_2/(2\tau_{i,2}). \quad (26)$$

432 *Extension to the tri-dimensional case*

433 While in the one-dimensional case the user chosen baseline, x , and the wind-drift
 434 velocity, \mathbf{V} , are always co-linear (because there is only one coordinate axis, the X axis), this
 435 is now no longer the usual case. In the tri-dimensional case, the user usually chooses a
 436 baseline, \mathbf{r} , which, under anisotropic conditions, is *in general* not aligned with the velocity
 437 vector, \mathbf{V} , and hence, the “natural” extension of Eq. (26) to $\mathbf{V} = \mathbf{r}/(2\tau)$ fails. In the following
 438 mathematical development, it will be shown that the idea behind the correlation-intersect
 439 method (Fig. 4) is that departing from a user baseline, $\mathbf{r} = \mathbf{r}_1$ (in general, not aligned with the
 440 wind velocity) is used to find an auxiliary vector, $\mathbf{V}_A = \mathbf{r}_1 - 2\mathbf{V}\tau_i$ (i.e., function of time-lag
 441 intersect τ_i). Once subtracted from the user’s proposed baseline, \mathbf{r}_1 , we obtain a new vector,
 442 $\mathbf{r}_1 - \mathbf{V}_A$, proportional to the maximum-correlation baseline, \mathbf{r}_{opt} (Fig. 4a). This new vector is
 443 then aligned with the true wind-drift direction, \mathbf{V} . In doing so, classic *spatial* correlation
 444 maximization is replaced by the *temporal* correlation intercept method, which does not require
 445 function maximization.

446 *Mathematical discussion* begins with definition of the frozen-atmosphere correlation
 447 function in absolute coordinates for baseline, \mathbf{r} , and time lag, τ , which is obtained by
 448 substituting Eq. (12) into Eq. (8) as

449
$$R_Z(\mathbf{r}, \tau) = f\left[\left(\mathbf{r}^T - \mathbf{V}^T \tau\right) \mathbf{A}(\mathbf{r} - \mathbf{V} \tau)\right]. \quad (27)$$

450 From Eq. (27), the temporal auto-correlation function is given by baseline $r = 0$ as

451
$$R_Z(\mathbf{0}, \tau) = f\left(\mathbf{V}^T \mathbf{A} \mathbf{V} \tau^2\right). \quad (28)$$

452 The correlation-intersect method between *temporal* auto- and cross-correlation functions is
453 formulated as

454
$$R_Z(\mathbf{r}, \tau_i) = R_Z(\mathbf{0}, \tau_i), \quad (29)$$

455 where subindex “i” stands for “intersect”.

456 Because the model decay function, f , is by definition the same for both auto- and
457 cross-correlation functions (Eqs. (27)-(28) above), equality condition, Eq. (29), can be directly
458 imposed over the respective f-function arguments as

459
$$\left(\mathbf{r}^T - \mathbf{V}^T \tau\right) \mathbf{A}(\mathbf{r} - \mathbf{V} \tau) = \mathbf{V}^T \mathbf{A} \mathbf{V} \tau^2. \quad (30)$$

460 After simple algebraic manipulation and by using $\mathbf{V}^T \mathbf{A} \mathbf{r} \tau = \mathbf{r}^T \mathbf{A} \mathbf{V} \tau$ (this term is a scalar), one
461 obtains

462
$$\mathbf{r}^T \mathbf{A}(\mathbf{r} - 2\mathbf{V} \tau) = 0. \quad (31)$$

463 Eq. (31) (to be numerically solved later) is the sought-after key equation enabling
464 retrieval of the wind-drift velocity. This equation can physically be interpreted as the dot
465 product between two vectors (vectors as columns); namely, $\mathbf{V}_A = \mathbf{r} - 2\mathbf{V} \tau$ and $\mathbf{V}_B = \mathbf{A} \mathbf{r}$, with
466 two possible solutions:

467
$$\mathbf{V}_A^T \mathbf{V}_B = 0 \Rightarrow \begin{cases} \mathbf{V}_A \perp \mathbf{V}_B \Rightarrow (\mathbf{r} - 2\mathbf{V} \tau) \perp \mathbf{A} \mathbf{r} \\ \mathbf{V}_A = \mathbf{0} \Rightarrow \mathbf{V} = \frac{\mathbf{r}}{2\tau} \end{cases}, \quad \tau = \tau_i. \quad (32)$$

468 Given a time-lag intercept, $\tau = \tau_i$, a particular solution, $\mathbf{V} = \mathbf{r}/(2\tau)$, stands for the very
 469 uncommon case in which the user chosen baseline coincides with the wind-drift velocity
 470 direction. This reduces to $\mathbf{V} = \mathbf{r}/(2\tau_i)$ in the Briggs' one-dimensional solution. Except for
 471 this particular case, the “correlation intercept method” must be explained from the general
 472 solution, $\mathbf{V}_A \perp \mathbf{V}_B$, depicted in Fig.4b. Because the baseline, $\mathbf{r} = \mathbf{r}_1$, is user-defined, the
 473 anisotropy matrix, \mathbf{A} , is known from Sect. 3.2. So is the vector \mathbf{V}_B . From the definition of
 474 \mathbf{V}_A above, the wind-drift velocity can be expressed as

$$475 \quad \mathbf{V} = \frac{1}{2\tau_{i,1}}(\mathbf{r}_1 - \mathbf{V}_A), \quad (33)$$

476 where we have substituted the user baseline, $\mathbf{r} = \mathbf{r}_1$, and time-lag intercept, $\tau = \tau_{i,1}$, for which
 477 $\mathbf{V}_A \perp \mathbf{V}_B$. From Eq. (33) it emerges that the vector $(\mathbf{r}_1 - \mathbf{V}_A)$ is aligned with velocity vector,
 478 \mathbf{V} (Fig. 4a), which, therefore, means that $\mathbf{r}_1 - \mathbf{V}_A$ is a vector proportional to the maximum-
 479 correlation baseline, \mathbf{r}_{opt} . By comparing Eq. (33) with Eq. (25), Eq. (33) can be rewritten as

$$480 \quad \mathbf{V} = \frac{\mathbf{r}_{opt}}{\tau_{i,1}}, \quad \mathbf{r}_{opt} = \frac{1}{2}(\mathbf{r}_1 - \mathbf{V}_A), \quad (34)$$

481 which re-encounters the well-known wind-drift velocity solution using spatial correlation
 482 maximization with baseline, \mathbf{r}_{opt} , and time lag, $\tau = \tau_{i,1}$.

483 A numerical solution for Eq. (31) is reached by rewriting it in the form of the scalar
 484 equation as

$$485 \quad \mathbf{r}^T \mathbf{A} \mathbf{r} = 2\tau_i (\mathbf{r}^T \mathbf{A} \mathbf{V}), \quad (35)$$

486 where we have used $X + X^T = 2X$, with X as the scalar quantity $X = \mathbf{r}^T \mathbf{A} \mathbf{V}$. The left term
 487 of Eq.(35) is easily identified in Eq.(20) and can be computed as the f -argument of the
 488 *measured* correlation function, $\Gamma_z(\mathbf{r}, 0)$. Substitution of Eq.(20) into Eq.(35) yields the
 489 numerical equation for the retrieval of the wind vector as

$$490 \quad \mathbf{r}^T \mathbf{A} \mathbf{V} = \frac{1}{2\tau_i} f^{-1}[\Gamma_z(\mathbf{r}, 0)]. \quad (36)$$

491 When Eq.(36) is evaluated for a set of baselines, $\mathbf{r} = \mathbf{r}_k$, $k = 1..M$ ($M \geq 3$), it is similar to
 492 Eq.(21). Therefore, the wind vector (in absolute coordinates) can be inverted from the $M \times 3$
 493 linear equation system as

$$494 \quad \mathbf{Q} \mathbf{V} = \mathbf{c}, \quad (37)$$

495 where $\mathbf{Q} = \mathbf{r}_k^T \mathbf{A}$ is the $M \times 3$ matrix defined by the product of the baseline vector, \mathbf{r}_k^T , the
 496 anisotropy matrix, \mathbf{A} , $\mathbf{V} = (V_x, V_y, V_z)$ is the wind vector to solve, and $\mathbf{c} = f^{-1}[\Gamma_z(\mathbf{r}_k, 0)]/2\tau_{i,k}$
 497 is the independent term defined by the f -argument of the spatial correlation function at zero
 498 time delay. $\tau_{i,k}$ is the intersecting time point from Eq.(29) for the \mathbf{r}_k baseline, which in
 499 practice is computed as $\Gamma_z(\mathbf{r}_k, \tau_{i,k}) = \Gamma_z(\mathbf{0}, \tau_{i,k})$.

500 Once \mathbf{V} is known, we compute the coordinate transform matrix, $\mathbf{\Psi}$, from the wind
 501 azimuth angle, ϕ_w , and Table 1. This enables recovery of the anisotropy matrix, \mathbf{M} (Eq.(5),
 502 from its rotated version, \mathbf{A} , derived in Sect. 3.2.

503 Using 1) $\mathbf{U} = \mathbf{\Psi}^{-1}\mathbf{V}$ (Table 1), 2) $\mathbf{\Psi}^{-1} = \mathbf{\Psi}^T$ ($\mathbf{\Psi}$ is unitary) and 3) that the cross-wind
 504 component is $U_2 = 0$ (by definition of the wind-relative coordinate system), it follows that the
 505 mean wind component is

$$506 \quad U_1 = \sqrt{V_x^2 + V_y^2}, \quad (38)$$

507 and the wind azimuth angle ϕ_w is

$$508 \quad \phi_w = \tan^{-1}\left(\frac{V_y}{V_x}\right). \quad (39)$$

509 The vertical wind component $U_3 = V_z$ remains invariant. Finally, $\mathbf{M} = \mathbf{\Psi}^T \mathbf{A} \mathbf{\Psi}$ is computed
 510 from Eq.(11).

511 4. Simplified application case

512 The wind-retrieval method presented in Sect. 3 has been applied to a two-angle azimuth scan
 513 (2AAS) scheme (2 LOS, $\phi = 225$ deg and $\phi = 228$ deg in azimuth, elevation $\theta = 40$ deg) using
 514 both isotropic and anisotropic models for comparison. In contrast to the three-angle azimuth
 515 scan (3AAS) often used in the literature (Kunkel et al., 1980; Buttler et al., 2001), which
 516 offers a higher number of redundant (coplanar) baselines, the 2AAS (Fig. 1) enables faster
 517 scan rates.

518 Measurements were obtained 1200-1205 UTC on 19 September 2008 with the RSLAB
 519 (Remote Sensing Lab) lidar operated at 1064 nm. Because the scattering cross sections of
 520 aerosols typically follow a λ^{-1} spectral dependency (λ^{-4} for molecules), the measurements
 521 benefit from a comparatively higher aerosol backscatter component than the molecular one at

522 the operating wavelength (Collis and Russell, 1976). The system uses a Nd:YAG 20-Hz laser
523 source with 160-mJ energy and 6-ns width pulses along with a 20-cm aperture, 2-m focal-
524 length telescope and 3-mm avalanche-photodiode-detector (APD)-based receiving channel
525 (7.5-m range resolution, Noise Equivalent Power $\approx 4.2 \times 10^{-13} \text{ W} \cdot \text{Hz}^{-1/2}$). The lidar was aimed
526 at 225-deg in azimuth corresponding with the southwest (SW) direction (north 0-deg, east 90-
527 deg convention) along a 40-deg elevation slant path. The scanning period was 4 s, consisting
528 of 1-s integration time (20 pulses) per LOS and 1-s dead time per LOS (moving time from one
529 azimuth to the other). Coincident potential temperature and relative humidity radio-soundings
530 at 1200 UTC, collected 600 m southeast (SE) from the lidar, are used to cross-examine the
531 results. Wind-velocity and direction information are derived from internal GPS measurements
532 coupled with the radiosonde measurements (VaisalaTM, mod. RS92-SGP).

533 *4.1. Practical aspects*

534 The atmospheric vertical profile (Z) has been divided into piece-wise homogeneous velocity-
535 inversion layers (see Sect. 2.2.1) of approximately 34 m depth (vertical inversion resolution),
536 corresponding with seven range bins (one bin equal to 7.5 m slant path) along the LOS of the
537 lidar instrument. In each vertical layer, Eq.(23), Sect. 3.2 and Eqs.(37)-(39), Sect. 3.3 are
538 solved from a user-defined set of baselines formed by three “best” baselines.

539 The practical baseline selection procedure follows (Fig. 1c). First, in a given layer, all
540 possible cross-correlations ($\Gamma_z^{pq,ij}(0)$; see Eq.(13) for notation) arising from combining two-
541 by-two the available data points in the velocity-inversion volume are computed from the
542 normalized lidar signals, S_n (Eq.(14)). This implies that aerosol content fluctuations must

543 exist in the atmosphere and be intense enough to be recorded in S_n . Second, three correlation
544 subsets are formed: (i) transversal correlations (i.e., correlations between points belonging to
545 different LOS) with a baseline parallel to the X axis, (ii) transversal correlations with a
546 baseline non-parallel to the X axis, and (iii) radial correlations, which by definition have the
547 baseline following a common LOS. Finally, the three “best” baselines are those giving the
548 absolute maximum of $\Gamma_z^{pq,ij}(0)$ in each of the subsets above. This baseline selection scheme
549 enables choice of a baseline parallel to the X axis, another one almost parallel to the Y axis,
550 and a third one following the apparent wind direction.

551 In the present 2AAS case example, because two LOS always lie on a plane, the wind-
552 retrieval method cannot retrieve the three-dimensional spatial anisotropy matrix (six non-null
553 coefficients in Eq.(5). Equivalently, the \mathbf{a} vector in Eq.(24)) nor the three wind components.
554 Therefore, for data sufficiency, the anisotropic model of Eq.(5) must somehow be simplified.
555 According to Mayor et al. (2003), a wind-oriented anisotropic pattern is expected to be found
556 at the bottom of the ABL, whereas this tendency vanishes towards an isotropic one in the
557 mixed layer. Anisotropic models can be considered for the 2AAS besides the isotropic one. A
558 “*horizontal anisotropy*” model applies to low-elevation scans (as an approach to the
559 horizontal-scan case) or, in general, to positions whose vertical distance, z , is small enough
560 inside the layer to consider the vertical variation of the spatial correlation negligible. Under
561 this assumption the anisotropy matrix, \mathbf{M} (Eq.(5)), reduces to a 2×2 matrix, since the
562 coefficients related to the variation in the vertical dimension are zero ($m_3 = 0$, $m_{13} = m_{23} = 0$).

563 The absolute-coordinate anisotropy matrix, \mathbf{A} , is also 2×2 and has three non-null coefficients
564 (a_x, a_y, a_{xy}) that can be determined (Sect. 3.2).

565 Computationally, once the wind vector and the anisotropy matrix, \mathbf{M} , are obtained, \mathbf{M}
566 is diagonalized. According to Horn and Johnson (1985) and Fig. 3, the eigenvectors of \mathbf{M} , \mathbf{e}_1 ,
567 and \mathbf{e}_2 are the principal axes of the correlation ellipse. The major axis corresponds with the
568 largest correlation length, and is representative of the highest correlation direction of the
569 aerosol field. The elongation or axial ratio of the correlation ellipse is the ratio between its
570 major and minor axes. The tilt is the deviation angle between the major axis and the wind
571 direction.

572 The simplified anisotropic model above is a step beyond the usual isotropic
573 assumption, for the degree of isotropy of the aerosol structures to be evaluated, instead of
574 assuming it "a priori". The functional model used for the aerosol spatial correlation function, f
575 in Eq.(3), was a unit-normalized decreasing exponential, $f(x) = \exp(-x)$, so that $B(\boldsymbol{\rho})$ in
576 Eq.(3) was Gaussian and the space-time aerosol correlation model function, $R_z(\boldsymbol{\rho}, \tau)$ in
577 Eq.(8) was a time-delayed Gaussian. The 1-s instrumental delay time between the two LOS
578 was offset by delaying the temporal LOS cross-correlations by the same time amount.

579 *4.2. Experimental results*

580 Fig. 5 shows the measured range-corrected power lidar profiles as time-height images for the
581 two LOS of the 2AAS for an observation time of 240 s (60 time records per LOS, $M=60$ in
582 Eq.(14)). Three different tendencies are evident. First, between 400 and 1000 m ASL (above

583 sea level) aerosol patterns appear sooner for the 225-deg LOS (Fig. 5a) than for the 228-deg
584 LOS (Fig 5b). There is slight radial motion outwards from the lidar. This is evidenced by
585 white solid circles at times $t_1 = 30$ s, $t_2 = 90$ s, $t_3 = 160$ s in Fig. 5a and, respectively, at times
586 $t'_1 = 45$ s, $t'_2 = 100$ s, $t'_3 = 170$ s in Fig. 5b. Second, between approximately 1200 and 1600 m
587 ASL, the situation reverses and the aerosol patterns appear sooner in the 228-deg LOS (Fig.
588 5b) than in the 225-deg LOS (Fig. 5a). This is indicated by circular shapes B_1 , B_2 and B'_1 , B'_2
589 in Fig. 5a and Fig. 5b, respectively, and reveals a wind-shear situation. Lastly, in the middle
590 region between approximately 850-1150 m there are less contrastable patterns to visually
591 identify the aerosol motion. Above 1600 m ASL, data are no longer represented, because of
592 the reduced signal-to-noise ratio (Fig. 6a) and absence of significant aerosols.

593 Fig. 6b depicts potential temperature and water vapor mixing ratio profiles from local
594 radiosonde. From the gradients of these profiles, the atmospheric boundary layer height is
595 found around 650 m, which is in agreement with the approximate mean height of the
596 contrasted structures in Fig. 5. Detection of such structures is usually limited to the ABL,
597 because it is characterized by a vigorous mixing and patchy structures of convective origin,
598 which give rise to relatively strong signal fluctuations. Transported aerosol layers above this
599 level tend to be fairly homogeneous, conveying meaningless signal fluctuations (i.e., noise)
600 once subtracted. In Fig. 5, inhomogeneities between 1200-1600 m in height are strong enough
601 to depict two structures, which has enabled our tentatively extending the study range above
602 the ABL up to 1600 m. The high relative humidity in the 1100-1400 m height interval can
603 increase the atmospheric optical backscatter through deliquescence of background aerosol
604 particles and haze activation (Tang, 1993) in Fig. 5. The large humidity gradient between 800

605 and 1200 m is symptomatic of wind shear, in contrast to the usual convective ABL near solar
606 noon.

607 Fig. 7 a,b shows the results of the wind-retrieval method using both the isotropic and
608 the anisotropic model. Fig. 7b shows profiles of the horizontal wind direction depicting a
609 wind-shear phenomenon caused by two air masses with different relative humidity (80%
610 below 800 m and up to 90% between 800-1400 m, Fig. 7b). For the lowermost height interval
611 (< 900 m), the data in Fig. 7a,b show little variation in estimates of horizontal wind speed and
612 direction. Both an/isotropic models retrieve similar estimates (in accordance with the radio-
613 sounding), though the isotropic estimates for wind speed are biased slightly low when
614 compared with the radiosonde. The wind-retrieval results for the uppermost height interval
615 (1200-1600 m) depict wind shear from 135 to 330 deg, which is identified by the anisotropic
616 model. This is not, however, the case for the isotropic model, which oscillates over some 300-
617 deg uncertainty, thus giving divergent wind-speed estimates. In the middle layer (850-1150
618 m), which is characterized by low aerosol content, performance of the anisotropic model,
619 particularly in the retrieval of the wind direction, is again better than that of the isotropic
620 model, and shows a progressive change in the wind direction (120 to 150 deg). But it is not as
621 accurate as the radiosonde. One reason accounting for this discrepancy is the lack of
622 significant aerosol content in this layer and low signal-to-noise ratio.

623 Fig.7 c,d shows the horizontal anisotropy of the aerosol structures in each horizontally
624 homogeneous layer of the wind profile (Sect. 2.2.1.1). The axial ratio is found to be between
625 unity (1:1) and ten (10:1), progressively increasing with height (notation $\rho_{c,1} : \rho_{c,2}$, note that
626 $m_3 = 0$, $m_{13} = m_{23} = 0$ in Eq.(5)), which resulted in a oblate ellipsoid for the quadratic function

627 model, $q(\boldsymbol{\rho})$ (Eq.(4)). Up to 750 m, the axial ratio lies between 1 and 3. In the 800-1100 m
628 height interval, which is characterized by less contrasted aerosol patterns, the ratios are
629 roughly between 2 and 5, and show higher dispersion. Finally, in the transported aerosol layer
630 aloft (1150-1400 m), the ratio is around 5. In each of these three intervals, the tilt angle is less
631 than 30-deg clockwise. In relation to Fig. 2, the elongated aerosol structures are not perfectly
632 (but almost) aligned with the wind direction, thus revealing a slight departure from the
633 isotropic assumption. In the stratified aerosol layer at 1100-1400 m, the ellipse elongation
634 increases.

635 5. Conclusions

636 Large-scale aerosol concentration gradients can effectively be sensed by multiple-lines-of-
637 sight (LOS) scanning backscatter lidars, thus allowing for the detection of anisotropic
638 patterns. A *three-component* low-troposphere wind-retrieval method under anisotropic media
639 has been formulated for backscatter-lidar scanning schemes consisting of a reduced number of
640 LOS. Classic spatial function maximization, which under the requirement of a densely
641 sampled volume (LOS in many different directions) in anisotropic conditions can yield the
642 true wind velocity, has been replaced by a temporal-correlation intersect method. The latter
643 does not require function maximization or a densely sampled volume. In contrast, a few LOS
644 (as in the multiple-angle azimuth scheme) with densely sampled measurements along them are
645 needed. A further result of the proposed method is that the matrix linear solution form is
646 obtained.

647 The method assumes a piece-wise “frozen” atmosphere divided into time-stationary
648 and statistically-homogeneous vertical layers (Sect. 2.2.1.1). The algorithm is mainly intended
649 for unstable convective boundary layer conditions and, therefore, usually limited to the
650 atmospheric boundary layer (ABL). However, the only inherent limitation is that aerosol
651 content fluctuations must exist in the atmosphere and be properly recorded in the mean-
652 subtracted range-corrected signal, S_n . That is, S_n must have acceptable signal-to-noise ratio
653 (SNR), (an instrument requirement), and enough signal variance (an atmospheric requirement)
654 to fairly reproduce aerosol fluctuations.

655 The space-time correlation function in an atmospheric aerosol layer (or velocity-
656 inversion volume) at height Z is estimated from the *temporal correlation* of range-corrected
657 lidar signals measured at non-colinear *baselines* (difference position vector between two
658 measurement points of a same/different LOS). Therefore, the baselines sample the velocity-
659 inversion volume along different directions in space and with different lengths in such a way
660 that the movement of the aerosol inhomogeneities swept away by the wind can be effectively
661 monitored.

662 Because the temporal correlation function computed from a baseline, \mathbf{r}_k , $k = 1..N$
663 (Fig. 2), $\Gamma_z(\mathbf{r}_k, \tau)$ depends on both the wind vector and the anisotropy of the medium, the
664 algorithm must correct for the “false-velocity” effects caused by the anisotropy. This is done
665 in two steps. First, the rotated anisotropy matrix, \mathbf{A} , is obtained from time cross-correlations
666 evaluated at zero-lag delay at different baselines. Second, the wind vector is obtained from the
667 temporal auto- and cross-correlation functions (full correlation analysis) and the rotated

668 anisotropy matrix. Since the wind-relative coordinate system is by definition aligned with the
669 wind direction, once the wind vector is known so is the rotation angle between both
670 coordinate systems and the aerosol anisotropy matrix, \mathbf{M} , can be obtained from the rotated
671 one, \mathbf{A} . This enables the anisotropy axial ratio and tilt angle of the correlation ellipse to be
672 computed with respect to the wind direction. In the tri-dimensional case, a minimum of $N = 6$
673 independent baselines (equivalently, six linear equations) is required to invert the rotated
674 anisotropy matrix, \mathbf{A} , and a minimum of $M = 3$ independent baselines to invert the wind
675 vector.

676 A first application of the method to a simplified two-angle-azimuth-scan (2AAS),
677 using both an/isotropic models, has shown the outperformance of the wind-retrieval
678 anisotropic method. With SNRs ranging from 40 to 6 along the measurement range, the
679 horizontal wind component, as well as anisotropic parameters inside the ABL and in an
680 aerosol layer aloft, have been retrieved (axial ratios between 1 and 10 and tilt angles between
681 0 and -30 deg). The anisotropic ratios obtained are substantially different from the “spherical”
682 case, so that the horizontal aerosol anisotropy was relevant enough so as to justify the
683 application of the anisotropic model in the wind-retrieval method presented. This is
684 corroborated by the finer and convergent results of the anisotropic model in Fig. 7. When
685 comparing them to radiosonde data in the $[400 - 800] \cup [1200 - 1600]$ -m range interval, where
686 there is significant aerosol loading, we have:

- 687 • In the 400-to-800-m range (range interval with high SNR, typically, $\text{SNR} \gg 10$)
688 approximate wind-speed and wind-direction *rms errors* are 1.0 m/s and 25.0

689 deg, respectively, for the anisotropic model; and 1.2 m/s and 24.0 deg, for the
690 isotropic model.

691 • In the 1200-to-1600-m range (range interval with low SNR, typically,
692 SNR<10), 3.5 m/s and 49.0 deg for the anisotropic model; and, as large as 9.2
693 m/s and 83.0 deg, for the isotropic model.

694 All considered, reasonable wind velocity information can be inverted as well as on
695 anisotropic parameters. Future research is to comprise closer study of error bounds within the
696 system.

697 *Acknowledgments*

698 The data for the application case of Sect. 4 was obtained at the Remote Sensing Lab
699 (RSLAB), UPC (<http://www.tsc.upc.edu/rs>) and it is available upon request from S. Tomás,
700 tomas@ice.cat.

701 This work was supported by the Spanish Ministry of Economy and Competitiveness
702 (MINECO) and European Regional Development Funds (FEDER) through UPC projects
703 TEC2012-34575 and TEC2009-09106 and ICE-CSIC project AYA2011-29183-C02-02 and,
704 in part, by the European Union through project ITARS (Initial Training in Atmospheric
705 Remote Sensing), GA-289923. MINECO is also thanked for S. Tomás' predoctoral fellowship
706 BES-2007-17047 when doing his Ph.D. at UPC.

707 The Astronomy and Meteorology Dep. of the Universitat de Barcelona provided the
708 daily radio-soundings used in the experimental part of this work.

709

710 **References**

711 ALADIN: Atmospheric Laser Doppler Instrument, ESA ed. SP-1112 (1989).

712

713 Astafurov, V. G., E. Y. Ignatova, and G. G. Matvienko, 1992: "Efficiency of lidar
714 measurements of wind velocity by a correlation lidar," *Atmos. Oceanic. Opt.*, **5**, 318.

715

716 Barlow, R. J., 1999: "Least Squares," Chap. 6 in *Statistics. A Guide to the Use of Statistical*
717 *Methods in Physical Sciences* (Wiley), pp. 97-117.

718

719 Briggs, B. H., G. J. Phillips and D. H. Shinn, 1950: "The Analysis of Observations on Spaced
720 Receivers of the Fading of Radio Signals," *Proc. Phys. Soc., Sect. B*, **63**, 106.

721

722 Briggs, B. H., 1968: "On the analysis of moving patterns in geophysics – I. Correlation
723 analysis", *J. Atmos and Terrestrial Physics*, **30**, 1777-1788.

724

725 Buttler, W., C. Soriano, J. Baldasano, and G. Nickel, 2001: "Remote Sensing of Three-
726 dimensional Winds with Elastic Lidar: Explanation of Maximum Cross-correlation Method,"
727 *Boundary-Layer Meteor.*, **101**, 305-327.

728

729 Clemesha, B. R., V. W. J. H. Kirchhoff, and D. M. Simonich, 1981: "Remote measurement of
730 tropospheric and stratospheric winds by ground based lidar," *Appl. Opt.*, **20**(17), 2907-2910.

731

732 Clifford, S. T., J. C. Kaimal, R. J. Lataitis, and R. G. Strauch, 1994: "Ground-Based Remote
733 Profiling in Atmospheric Studies: An Overview," *Proc. IEEE*, **82**(3), 313-355.
734

735 Collis, R.T.H. and P.B. Russell, 1976: "Lidar Measurement of Particles and Gases by Elastic
736 Backscattering and Differential Absorption," Chap.4 in *Laser Monitoring of the Atmosphere*,
737 E.D. Hinkley, Ed., pp. 71-102, (Springer-Verlag, New York), pp.71-102.
738

739 Comerón, A., C. Muñoz, F. Rocadenbosch, A. Rodríguez, M. Sicard, and S. Tomás, 2010:
740 Lidar measurement of wind velocity fields. *Recent Advances in Atmospheric Lidars*, L.
741 Fiorani and V. Mitev, Eds., INOE Publishing House, Bucharest, Romania. ISBN 978-973-
742 88109-6-9.
743

744 Dérian, P., P. Héas, E. Mémin and S. D. Mayor, 2010: "Dense motion estimation from eye-
745 safe aerosol lidar data," *Proc. 25th International Laser Radar Conference*, St. Petersburg
746 (Russia), 5-9 July 2010 , Vol. 1, 377–380.
747

748 Doviak, R. J., R.J. Lataitis and C. L. Holloway, 1996: "Cross correlation and cross spectra for
749 spaced antenna wind profilers," *Radio Science*, **31**(1), 157-178.
750

751 Eloranta, E. W., J. M. King, and J. A. Weinman, 1975: "The determination of wind speeds in
752 the boundary layer by monostatic lidar," *J. Appl. Meteorol.*, **14**, 1485-1489.
753

754 Elperin, T., N. Kleorin and I. Rogachevskii, 1996: "Isotropic and anisotropic spectra of
755 passive scalar fluctuations in turbulent fluid flow," *Phys. Rev. E*, **53**(4), 3431-3441.
756

757 Ferdinandov, E. S. and T. A. Mitsev, 1982: "Effect of transparency fluctuations on the
758 accuracy of lidar correlation measurements of statistically inhomogeneous atmosphere," *Bulg.*
759 *J. Phys.*, **9**, 537.
760

761 Hall, F. F., Jr., R. M. Huffaker, R. M. Hardesty, M. E. Jackson, T. R. Lawrence, M. J. Post, R.
762 A. Ritcher, and B. F. Weber, 1984: "Wind measurement accuracy of the NOAA pulsed
763 infrared Doppler lidar," *Appl. Opt.*, **23**, 2503-2506.
764

765 Holloway, C.L., R.J. Doviak, S.A. Cohn, R.J. Latatis and J.S. Van Baelen, 1997: "Cross
766 correlation and cross spectra for spaced antenna wind profilers. Part II. Algorithms to estimate
767 wind and turbulence," *Radio Sci.*, **32**(3), 967-982.
768

769 Hooper, W. P., and E. W. Eloranta, 1986: "Lidar Measurements of Wind in the Planetary
770 Boundary Layer: The Method, Accuracy and Results from Joint Measurements with
771 Radiosonde and Kyttoon," *J. Appl. Meteorol.*, **25**, 990-1001.
772

773 Horn, R.A. and Johnson, C.R., 1985: *Matrix Analysis*, Section 7.3, Cambridge University
774 Press.
775

776 Huffaker, R. M., and R. M. Hardesty, 1996: "Remote Sensing of Atmospheric Wind
777 Velocities Using Solid-State and CO₂ Coherent Laser Systems," *Proc. IEEE*, **84**(2), 181-204.
778

779 Ishimaru, A., 1978: Scattering of waves from random continuous and turbulent media. *Wave*
780 *propagation and scattering in random media*. Vol. 2. Academic Press Inc, San Diego, CA, pp.
781 334-336.
782

783 Kolev, I., O. Parvanov and B. Kaprielov, 1988: "Lidar determination of winds by aerosol
784 inhomogeneities: motion velocity in the planetary boundary layer," *Appl. Opt.* **27**, 2524–2531.
785

786 Kovalev, V.A., and W. E. Eichinger, 2004: "Wind measurement methods from elastic lidar
787 data," in *Elastic Lidar: Theory, Practice and Analysis Methods*, John Wiley & Sons, Inc.,
788 521–529.
789

790 Kunkel, K. E., E. W. Eloranta, and J. A. Weinman, 1980: "Remote Determination of Winds,
791 Turbulence Spectra and Energy Dissipation Rates in the Boundary Layer from Lidar
792 Measurements," *J. Atmos. Sci.*, **37**, 978-985.
793

794 Kunz, G.J. (1996): "Field test of a lidar wind profiler," *Opt. Engineering* **35**(11), 3074–3083.
795

796 LAWS: Laser Atmospheric Wind Sounder: NASA Instrument Panel Report Vol.
797 IIg, Earth Observing System (1987).

798

799 Little, L. T., and R. D. Ekers, 1971: "A Method for Analysing Drifting Random Patterns in
800 Astronomy and Geophysics," *Astron. Astrophys.*, **10**, 306.

801

802 Matsui, I., N. Sugimoto, Y. Sasano, and H. Shimizu, 1990: "Wind Profiling by a Conical-
803 Scanning Time-Correlation Lidar," *Jpn. J. Appl. Phys.*, **29**, 441-444.

804

805 Mayor, S.D. and E. W. Eloranta, 2001: "Two-dimensional vector wind fields from volume
806 imaging lidar data," *J. Appl. Meteorol.*, **40**, 1331-1346.

807

808 Mayor, S. D., G. J. Tripoli, and E. D. Eloranta, 2003: "Evaluating Large-Eddy Simulations
809 using Volume Imaging Lidar Data", *Monthly Weather Review*, **131**, 1428-1452.

810

811 Mayor, S.D., 2010: "Horizontal motion vectors from cross-correlation: First application
812 to eye-safe aerosol lidar data from CHATS," *Proc. 25th International Laser Radar
813 Conference (ILRC)*, St. Petersburg (Russia), 5-9 July 2010, Vol. 1, 317–320.

814

815 Mayor, S. D., P. Dérian P., C. F. Mauzey, and M. Hamada, 2013: "Two-component wind
816 fields from scanning aerosol lidar and motion estimation algorithms," *Lidar Remote Sensing
817 for Environmental Monitoring XIV*, 25 August 2013, San Diego, (California, USA). *Proc.
818 SPIE*, 8872, 817208-1, 817208- 887208-16.

819

820 Measures, R. M., 1992: Laser Systems as Remote Sensors. *Laser Remote Sensing:*
821 *Fundamentals and Applications*, R. M. Measures, Ed., Krieger Publishing Company, Malabar,
822 Florida, 205-236.

823

824 Morley, B. W. Brown, and S. Spuler, 2010: Wind profiles with an elastic backscatter lidar
825 using auto and cross-correlation techniques, *25th Intl. Laser Radar Conference (ILRC)*, Vol.
826 1, 290-292, S2P-01.

827

828 Phillips, G. J., and M. Spencer, 1955: "The Effects of Anisometric Amplitude Patterns in the
829 Measurement of Ionospheric Drifts," *Proc. Phys. Soc., Sect. B*, **68**, 481.

830

831 Piironen, A.K. and E. W. Eloranta, 1995: "Accuracy analysis of wind profiles calculated from
832 volume imaging lidar data," *J. Geophys. Res.*, 100, 25559–25567.

833

834 Rocadenbosch, F., 2003: Lidar-Wind, Raman, and Other Sensing. *Encyclopedia of Optical*
835 *Engineering*, R. G. Driggers, Ed., Vol. 1, Marcel Dekker, New York, 1114-1127, DOI:
836 10.1081/E-EOE-120009505.

837

838 Sasano, Y., H. Hirohara, T. Yamasaki, H. Shimizu, N. Takeuchi, and T. Kawamura, 1982:
839 "Horizontal Wind Vector Determination from the Displacement of Aerosol Distribution
840 Patterns Observed by a Scanning Lidar," *J. Appl. Meteorol.*, **21**, 1516-1523.

841

842 Schwemmer, G. K., 1998, "Holographic Airborne Rotating Lidar Instrument Experiment,"
843 *Proc. 19th International Laser Radar Conference (ILRC)*, 6-10 July 1998, Annapolis
844 (Maryland, USA), 623–626.

845

846 Schols, J. L., and E. W. Eloranta, 1992: "Calculation of Area-Averaged Vertical Profiles of
847 the Horizontal Wind Velocity From Volume-Imaging Lidar Data," *J. Geophys. Res.*, **97**,
848 18395-18407.

849

850 Sroga, J. T., E. W. Eloranta, and T. Barber, 1980: "Lidar Measurement of Wind Velocity
851 Profiles in the Boundary Layer," *J. Appl. Meteorol.*, **19**, 598-605.

852

853 Stull, R. B., 1988: Governing equations for turbulent flow. *An Introduction to Boundary Layer*
854 *Meteorology*, Kluwer Academic Publishers (Dordrecht, The Netherlands), p.5 and pp. 75-114.

855

856 Sugimoto, N., I. Matsui, M. Pinandito, T. Ishii, S. Murata, and N. Yasuda, 1998: "An
857 Improved Method for Wind Measurements with a Conical-Scanning Correlation Lidar," *Jpn.*
858 *J. Appl. Phys.*, **37**, 5598-5603.

859

860 Tang, I. N. and H. R. Munkelwitz, 1993: "Composition and temperature dependence of the
861 deliquescence properties of hygroscopic aerosols," *Atmos. Environ.*, **27A**, 467–473.

862

863 Taylor, G. I., 1938: "The spectrum of turbulence," *Proc. Roy. Soc. London*, A132, 416–490.

864

865 Wilkerson, T.D., C.Q. Egbert, I.Q. Andrus, and M.E. Anderson, 2002: "Advances in Wind
866 Profiling by Means of Lidar and Video Imagery of Clouds and Aerosols," Laser Radar
867 Technology and Applications VII, 3-4 April 2002, Orlando (Florida, USA), *Proc. of SPIE*,
868 4723, 130–146.

869

870 Young, P. and E.W. Eloranta, 1995: "Calculation of divergence and vertical motion from
871 volume-imaging lidar data," *J. Geophys. Res.*, 100, D12, 25577–25583.

872

873 Zuev, V. E., Y. M. Vorevodin, G. G. Matvienko, and I. V. Samokhvalov, 1977: "Investigation
874 of structure and dynamics of aerosol inhomogeneities in the ground layer of the atmosphere,"
875 *Appl. Opt.*, **16**(8), 2231-2235.

876

877

878 **List of Figures**

879 Fig. 1. Geometry of the problem and coordinate systems. (a) Sketch of the lidar scanning scheme
880 along two generic LOS, LOS-1 (θ_1, ϕ_1) and LOS-2 (θ_2, ϕ_2) with θ_i and $\phi_i, i=1,2$ their respective
881 elevation and azimuth angles. (b) Coordinate systems. In an atmospheric layer $(Z_a \leq Z \leq Z_b)$, the
882 wind-relative coordinate system $(\hat{x}_1, \hat{x}_2, \hat{x}_3)$ is defined so that \hat{x}_1 is aligned with the wind direction
883 (\hat{x}_1 parallel to \mathbf{U}_1 , Eq.(1)). The lidar-absolute coordinate system has \hat{y} aligned with the
884 horizontal projection of the bisectrix of the angle between the two LOS. ϕ_w is the azimuth
885 rotation angle between both coordinate systems. (c) Detail of an atmospheric layer $(Z_a \leq Z \leq Z_b)$
886 or velocity-inversion volume (LOS_p and LOS_q are two generic LOS). Dots represent the lattice of
887 lidar measurement datapoints. Notation (p, i) indicates LOS_p and i -th measurement point.
888 Baseline $\mathbf{r} = \mathbf{r}_{pq,ij}$ is defined by measurement points (p, i) and (q, j) . (1) and (2) are transversal
889 baselines, (3) is a radial baseline (see Sect. 4.1).

890

891 Fig. 2. Illustration of the anisotropy (Z axis exits from the paper). The Y axis and the dashed
892 arrowed line represent two LOS. \mathbf{r}_{12} , \mathbf{r}_{13} , and \mathbf{r}_{23} are the baselines associated to measurement
893 points, $P_1 \dots P_3$. The size of the aerosol structures sensed at these measurement points is large
894 enough to be assumed anisotropic. Anisotropy gives rise to elliptic contours of the spatial
895 correlation function. \mathbf{e}_1 and \mathbf{e}_2 are the major and minor axis, respectively, of the characteristic
896 ellipse. Note that the correlation axis \mathbf{e}_1 is neither aligned with the wind direction \hat{x}_1 (Eq.(1))

897 nor with the baselines. The orientation of the ellipse with respect to the wind direction is the tilt
898 angle α .

899

900 Fig. 3. Contours of constant correlation $R_z(x, \tau) = \text{const.}$ as rotated concentric ellipses under the
901 one-dimensional case (X-axis).

902

903 Fig. 4. Vector representation of Eq. (32) general solution, $\mathbf{V}_A \perp \mathbf{V}_B$. (a) Concept idea of auxiliary
904 vector, \mathbf{V}_A . (b) Detail of vector \mathbf{V}_A for the time-lag intersect solution, $\tau = \tau_{i,1}$, giving
905 $\mathbf{V}_A = \mathbf{r}_1 - 2\mathbf{V}\tau_{i,1}$. \mathbf{V} is the wind-drift velocity vector and $\mathbf{r} = \mathbf{r}_1$ is the user's baseline. $\mathbf{V}_B = \mathbf{A}\mathbf{r}_1$
906 is the anisotropy-rotated baseline.

907

908 Fig. 5. Two-angle azimuth time-height images of the mean-subtracted range-corrected lidar
909 signal, $S_n(R, t)$ (Eq.(14)) corresponding to September 19, 2008, 1200-1205 UTC, $\theta = 40$ deg,
910 $\phi_1 = 225$ deg, $\phi_2 = 228$ deg, 1064-nm wavelength. Each figure represents a LOS time-height
911 record.

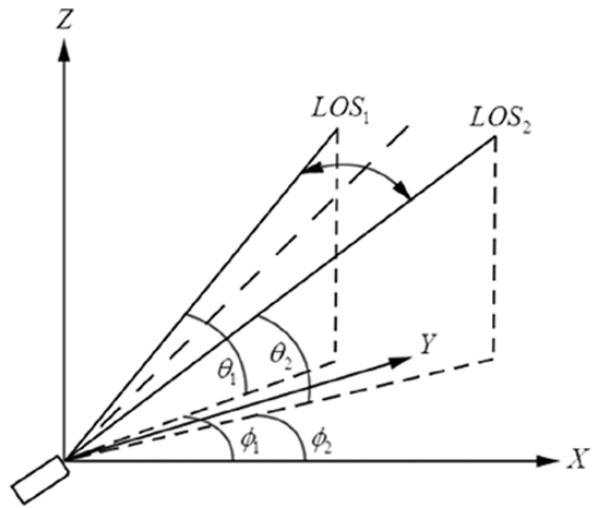
912

913 Fig. 6. Parameters associated to September 19, 2008 measurement (Fig. 5). (a) SNR estimate (1-
914 s time average). The shaded area (400-1600 m) indicates the wind-retrieval range. (b) Potential
915 temperature (solid line with crosses) and water vapour mixing ratio (solid line with void circles)
916 derived from 1200 UTC, radio-sounding data. The dashed line around 650 m indicates the
917 estimated mixing-layer depth.

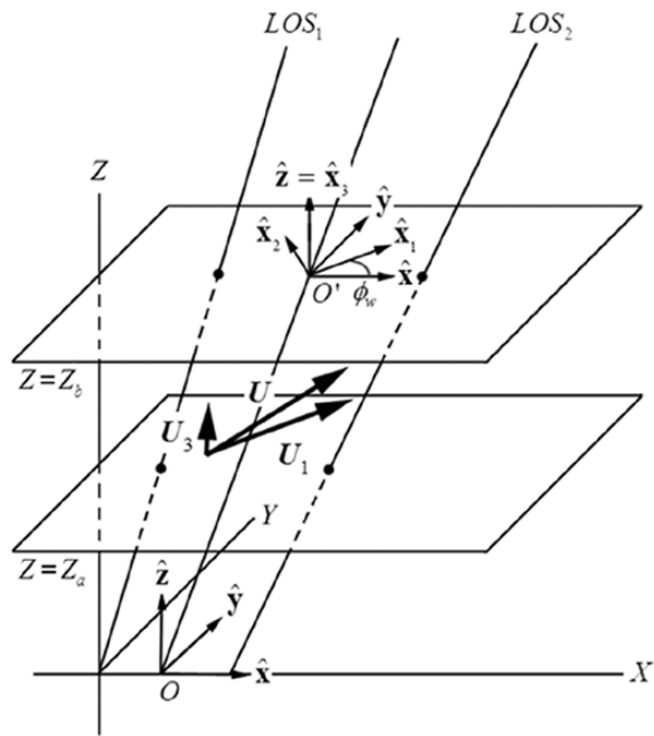
918 Fig. 7. Horizontal wind-velocity and horizontal-anisotropy estimates as a function of height. (a)
919 Horizontal wind speed, (b) wind direction. (Black trace, black circles) Estimates using the
920 horizontal anisotropic model (see Sect. 4.1). (Dashed trace, grey void circles) Estimates using the
921 isotropic model. (Grey trace, crosses) Radio-sounding data. (c, d) Retrieved horizontal-
922 anisotropy parameters: (c) Axial ratio, (d) tilt angle of the major axis of the correlation ellipse
923 with respect to the wind direction (α angle in Fig. 2). Horizontal dashed lines indicate height
924 intervals with similar anisotropic parameters.

Tables

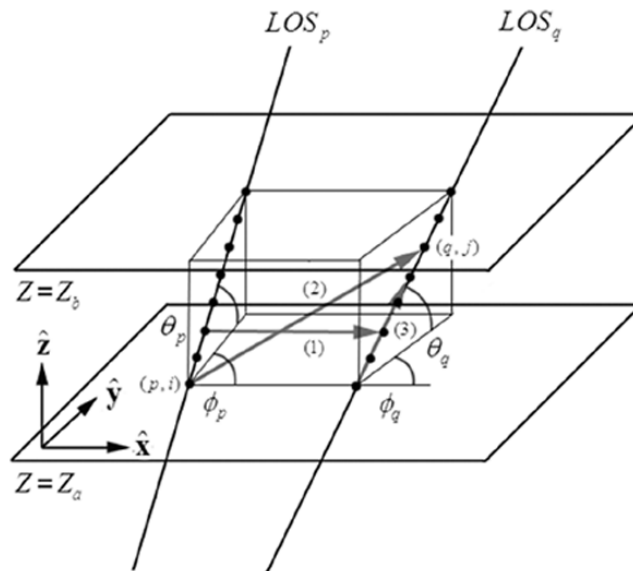
| VARIABLE | RELATIVE COORD. SYSTEM | ABSOLUTE COORD. SYSTEM |
|---|--|---|
| | $(\hat{\mathbf{x}}_1, \hat{\mathbf{x}}_2, \hat{\mathbf{x}}_3)$ | $(\hat{\mathbf{x}}, \hat{\mathbf{y}}, \hat{\mathbf{z}})$ |
| Range vector | $\mathbf{X} = X_1\hat{\mathbf{x}}_1 + X_2\hat{\mathbf{x}}_2 + X_3\hat{\mathbf{x}}_3 \rightarrow P[X_1, X_2, X_3]$ | $\mathbf{R} = X\hat{\mathbf{x}} + Y\hat{\mathbf{y}} + Z\hat{\mathbf{z}} \rightarrow P[X, Y, Z]$ |
| Baseline (difference) vector | $\boldsymbol{\rho} = \mathbf{X}_2 - \mathbf{X}_1 = (\rho_1, \rho_2, \rho_3)$ | $\mathbf{r} = \mathbf{R}_2 - \mathbf{R}_1 = (x, y, z)$ |
| Mean wind | $\mathbf{U} = U_1\hat{\mathbf{x}}_1 + U_3\hat{\mathbf{x}}_3$ | $\mathbf{V} = V_x\hat{\mathbf{x}} + V_y\hat{\mathbf{y}} + V_z\hat{\mathbf{z}}$ |
| Coordinate transform (range vectors) | $\mathbf{r} = \boldsymbol{\Psi}\boldsymbol{\rho}, \boldsymbol{\Psi} = \begin{pmatrix} \cos\phi_w & -\sin\phi_w & 0 \\ \sin\phi_w & \cos\phi_w & 0 \\ 0 & 0 & 1 \end{pmatrix}$ <p>(note that $\boldsymbol{\Psi} = \boldsymbol{\Psi}(\mathbf{U})$ via the wind angle ϕ_w)</p> | |
| Other relationships | $\mathbf{A} = \boldsymbol{\Psi}\mathbf{M}\boldsymbol{\Psi}^T$ (anisotropy matrix) | $\mathbf{V} = \boldsymbol{\Psi}\mathbf{U}$ (wind vector) |
| <p>Tab. 1 Variable definition for the relative and absolute coordinate systems used. Note that \mathbf{X} and \mathbf{R} (upper-case letters) stand for <i>range</i> vectors associated to point P whereas $\boldsymbol{\rho}$ and \mathbf{r} (lower case) stand for <i>baseline</i> vectors (i.e., difference position vectors).</p> | | |



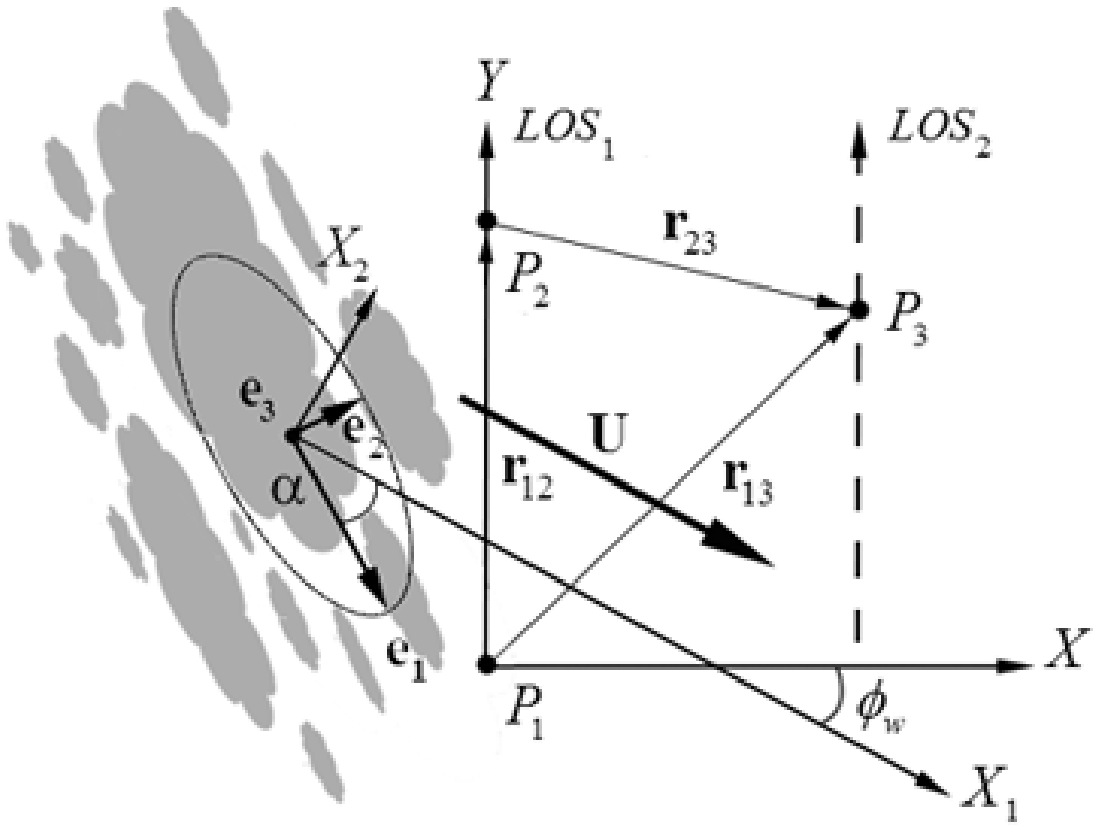
(a)

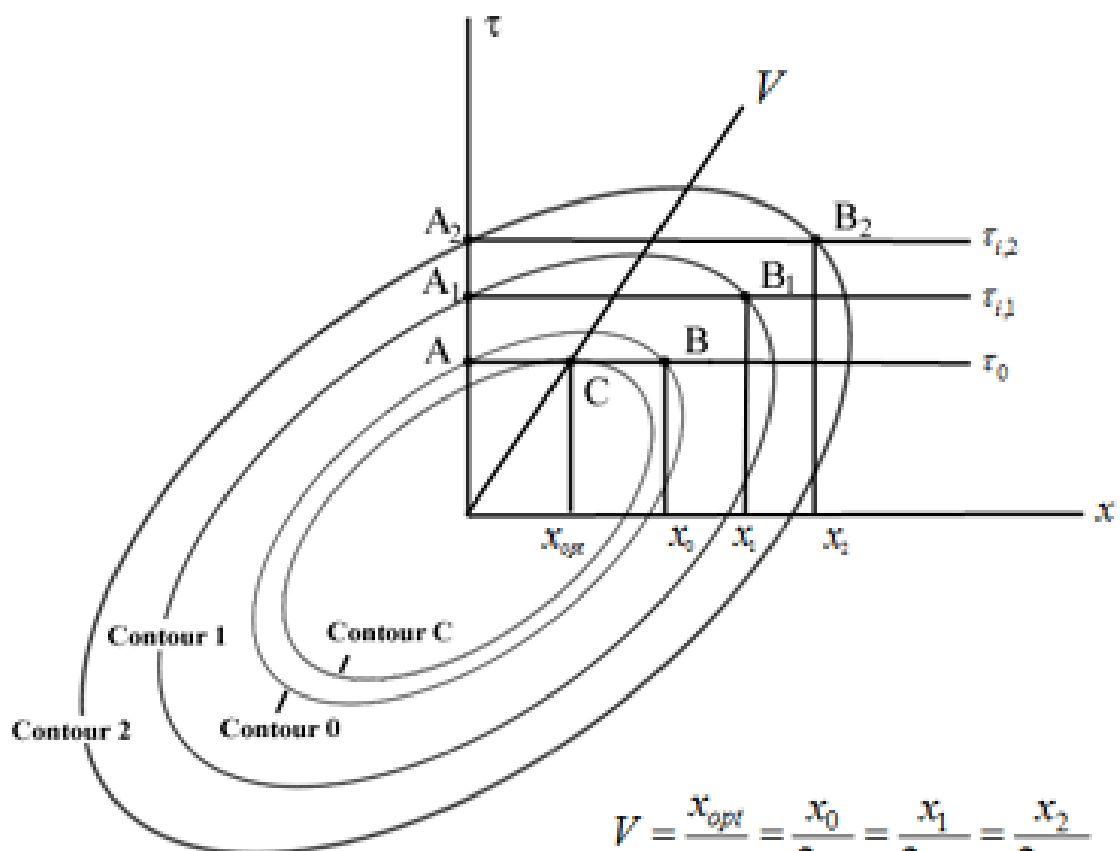


(b)

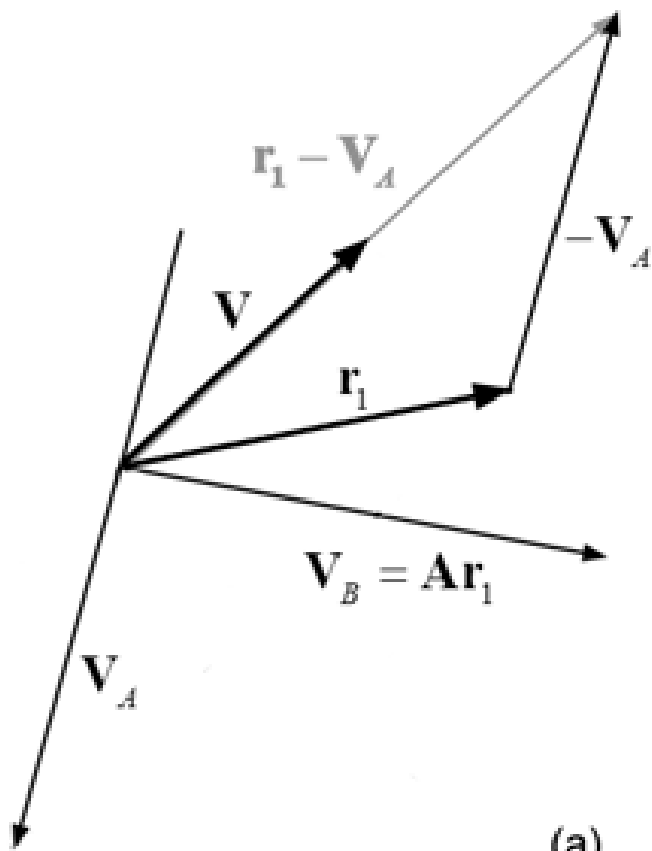


(c)

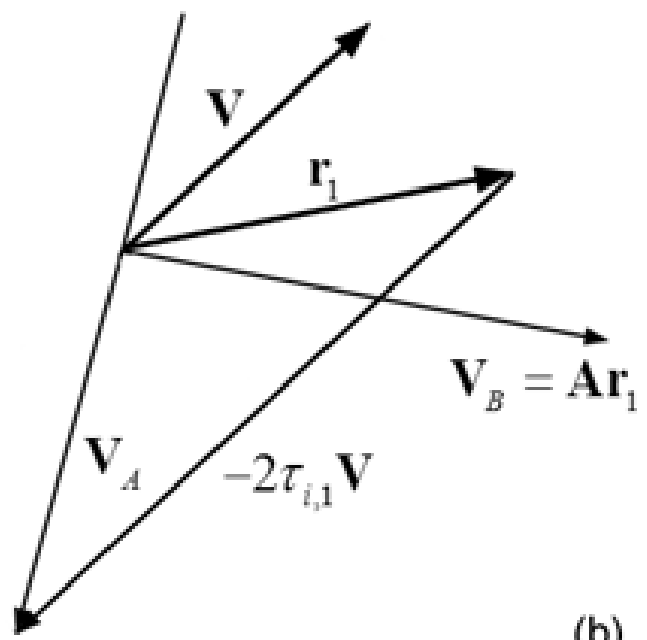




$$V = \frac{x_{opt}}{\tau_0} = \frac{x_0}{2\tau_0} = \frac{x_1}{2\tau_{i1}} = \frac{x_2}{2\tau_{i2}}$$



(a)



(b)

19-09-2008 - $\lambda = 1064$ nm
Start: 1200 UTC End: 1204 UTC

Azimuth= 225° Elevation= 40°

Azimuth= 228° Elevation= 40°

